Synthesis and Electrochemical Performance of Molybdenum Disulfide-Reduced Graphene Oxide-Polyaniline Ternary Composites for Supercapacitors

Li-Zhong Bai*, Yan-Hui Wang, Shuai-Shuai Cheng, Fang Li, Zhi-Yi Zhang and Ya-Qing Liu*

Shanxi Province Key Laboratory of Functional Nanocomposite Materials, North University of China, Taiyuan, China

Molybdenum disulfide/reduced graphene oxide/polyaniline ternary composites (MoS_2/rGO/PANI) were designed and synthesized by a facile two-step approach including hydrothermal and *in situ* polymerization process. The MoS_2/rGO/PANI composites presented an interconnected 3D network architecture, in which PANI uniformly coated the outer surface of the MoS_2/rGO binary composite. The MoS_2/rGO/PANI composites with a weight percent of 80% (MGP-80) exhibits the best specific capacitance ($570\,F\,g^{-1}$ at $1\,A\,g^{-1}$) and cycling stabilities (78.6% retained capacitance after 500 cycles at $1\,A\,g^{-1}$). The excellent electrochemical capacitive performance is attributed to its 3D network structure and the synergistic effects among the three components that make the composites obtain both pseudocapacitance and double-layer capacitance.

Keywords: molybdenum disulfide, reduced graphene oxide, polyaniline, ternary composites, supercapacitors

INTRODUCTION

To meet the burgeoning need of light-weight and portable electronic devices, efficient and environmentally-friendly electrochemical energy storage systems are urgently developed (Liu et al., 2017). Among the various energy storage systems, supercapacitors have drawn tremendous research attention due to their low cost, environmental friendliness, fast charging and discharging rate, excellent power density, high cycling stability, and long cycle life (Dunn et al., 2011; Yu et al., 2013; Wu et al., 2017; Qu et al., 2018). According to the charge-storage mechanism, supercapacitors are classified into two categories: electrochemical double-layer capacitors (EDLCs) and pseudocapacitors (Zhang et al., 2016). In general, pseudocapacitors of transition metal oxides and conducting polymers possess much higher specific capacitance than EDLCs of carbon materials, but their cycling stability is inferior (Li et al., 2014). Naturally, to draw on each other's strengths, a binary or ternary hybrid material composed carbon materials, a transition metal oxide and conducting polymer is more effective for high specific capacitance and long life time (Chen et al., 2014).

Graphene, a two-dimensional monolayer of sp^2 carbon atoms, is considered as an extremely promising candidate for future advanced applications in supercapacitors due to its excellent electrical conductivity, high surface area, good mechanical flexibility, and chemical

stability (Zhang et al., 2012). Meanwhile, it is an ideal substrate for the growth and anchoring of nanomaterials, such as metal oxide, metal sulfide and conducting polymers, to exploring hybrid composite for improved electrochemical properties (Zhao et al., 2018). Among various hybrid materials, graphene/MoS₂, graphene/PANI, MoS₂/PANI binary nanostructure are found to be promising electrode materials for supercapacitors (Ataca et al., 2012; Huang et al., 2013; da Silveira Firmiano et al., 2014; Thangappan et al., 2016). For example, Thangappan et al. reported a facile one step preparation of a molybdenum disulfide (MoS₂) nanosheet-graphene (MoS₂/G) composite with the *in situ* reduction of graphene oxide, which exhibited a high specific capacitance of 270 and 90 F g^{-1} at 0.1 and 1.0 A g^{-1}, respectively. In addition, its specific capacitance can still remain 89.6% after 1,000 cycles at 0.6 Ag^{-1} (Thangappan et al., 2016). However, three major defects found in the binary composite including the low practical capacitance, poor cycle stability and poor rate performance, hinder its wide application in supercapacitors (David et al., 2014).

Recently, a ternary composite of MoS₂/graphene wrapped with Fe₃O₄, polypyrrole and carbon nanotubes has been tried out in the fields of lithium ion batteries, electromagnetic wave absorption and electrocatalyst (Khan et al., 2016; Xie et al., 2016; Li et al., 2017). However, there are few reports on the synthesis of MoS₂/rGO/PANI ternary nanostructure for supercapacitors applications.

In this work, we prepared molybdenum disulfide/reduced graphene oxide/polyaniline (MoS₂/rGO/PANI) ternary composites by a facile two-step method. In the first step, the MoS₂ nanosheets are uniformly grown on the surface of the GO nanosheets through a hydrothermal process to produce a MoS₂/rGO binary composite. In the second step, the MoS₂/rGO/PANI ternary composites were synthesized by *in situ* polymerization of aniline on the out face of the MoS₂/rGO binary composite. In the MoS₂/rGO/PANI ternary composites, the weight percent of PANI can effectively improve their electrochemical performance when they serve as the electrode materials in supercapacitors. The results indicate that the MoS₂/rGO/PANI ternary composites deliver a very high specific capacity and excellent cyclic stability compared with the MoS₂/rGO binary composite.

EXPERIMENTAL

Synthesis of a MoS₂/rGO Binary Composite

Graphene oxide (GO) was synthesized from natural graphite flakes by a modified Hummers method (Zhang et al., 2015). The MoS₂/rGO binary composite was prepared by a facile hydrothermal method. Typically, GO (0.8 g), $(NH_4)_6Mo_7O_{24}\cdot4H_2O$ (1.236 g), thiourea (4 g) and HCl solution (0.2 ml) were dispersed in deionized water (40 ml) and sonicated for 1 h to form a uniform suspension. The above mixed dispersion was transferred into a Teflon-line stainless steel autoclave (50 ml) and annealed at 220°C for 18 h. After cooling down, the black precipitate was collected by centrifugation, washed with deionized water and ethanol for several times, and dried at 80°C for 24 h.

Synthesis of MoS₂/rGO/PANI Ternary Composites

The MoS₂/rGO/PANI ternary composites were synthesized by *in situ* polymerization in the presence of MoS₂/rGO and aniline. Typically, a certain amount of MoS₂/rGO and dodecyl benzenesulfonic acid (4.065 g) were dispersed into 50 ml deionized water with ultrasonic radiation. Aniline (1.16 g) and deionized water (75 ml) were poured into the above suspension and sonicated for 1 h. A solution of APS (0.5 M, 25 ml) was dropwise added to the above mixed dispersion and continually stirred at 0°C for 5 h and then at 20°C for 2 h. After that, the blackish green product was filtered and washed with acetone, and then dried in a vacuum oven at 60°C for 8 h. The resultant MoS₂/rGO/PANI ternary composites were denoted as MGP-X, where X (X = 50, 60, 70 and 80) represents the weight percentage loading of PANI in the ternary composites.

Material Characterization

The morphology and microstructure of the samples were characterized by a S-4800 scanning electron microscope (SEM) and a JEOL 2010 field-emission transmission electron microscope (TEM). The crystalline structures of the samples were performed on a Rigaku D/Max-2500 X-ray diffractometer with Cu Kα radiation (λ = 0.1542 nm) in the 2θ range from 5° to 90°. Fourier transform infrared (FT-IR) spectra were recorded on a Bruker Optics TENSOR 27 spectrometer using KBr pellets in the wave-number range of 400–4,000 cm^{-1}.

Electrochemical Measurements

The electrochemical performance of the samples used as electrode materials for supercapacitors were measured in a three-electrode system. The working electrodes were fabricated by mixing 80 wt% active materials, 10 wt% carbon black, and 10 wt% polytetrafluoroethylene (PTFE) solution. The mixture was pasted on stainless steel network (1 × 1 cm²) and dried at 80°C for 12 h in a vacuum oven. The mass of active materials loaded on the working electrodes were 4–5 mg. A platinum foil and a saturated calomel electrode (SCE) were used as the counter electrode and reference electrode, respectively, and 1 M H_2SO_4 aqueous solution was used as the electrolyte. Cyclic voltammetry (CV) tests were obtained at different scan rates (1, 2, 5, 10, 20, 50, and 100 mV s^{-1}) within a potential window of 0–1.0 V vs. SCE. Electrochemical impedance spectroscopy (EIS) measurements were carried out in the frequency range from 0.01 Hz to 100 KHz with 5 mV AC voltage amplitude at open circuit potential. Galvanostatic charge-discharge (GCD) investigations were performed at various current density (1, 2 3, 4, and 5 A g^{-1}) in a potential range of 0–1.0 V vs. SCE. The capacities of the samples were calculated based on the mass of the active materials.

RESULTS AND DISCUSSION

Structure and Morphology of MoS₂/rGO/PANI Ternary Composites

Figure 1 shows XRD patterns of the PANI, MoS₂/rGO binary composite, and MoS₂/rGO/PANI ternary composites,

respectively. The diffraction peaks of the PANI located at $2\theta =$ 20.3° and 25.3°, which can be assigned to (020) and (200) crystal planes of the emeraldine PANI salt, respectively (Tong et al., 2014). The MoS$_2$/rGO binary composite exhibits the diffraction peaks centered at $2\theta =$ 14.1°, 33.1°, 39.6°, and 58.9°, which can be ascribable to the (002), (100), (103) and (110) crystal planes of 2H-phase MoS$_2$ (JCPDS no. 37-1492), respectively. The diffraction peak of the rGO located at $2\theta =$ 26.5° cannot be detected in the MoS$_2$/rGO binary composite, which indicates that the restacking of graphene layers was inhibited by MoS$_2$ nanosheets (Wang et al., 2014; Dai et al., 2017). In the diffraction spectrum of the MoS$_2$/rGO/PANI ternary composites, there are some characteristic diffraction peaks of both MoS$_2$/rGO and PANI, revealing that the PANI is successfully attached onto the surface of the MoS$_2$/rGO binary composite. Moreover, the intensities of the diffraction peaks from PANI gradually increase with the elevated weight percent of PANI. All the results indicate that these three components are fully compounded together.

Figure 2 shows FT-IR spectra of the PANI, MoS$_2$/rGO binary composite, and MoS$_2$/rGO/PANI ternary composites, respectively. As shown in **Figure 2**, the spectrum of PANI shows strong absorption peaks at 1,120, 1,250, 1,310, 1,489, and 1,550 cm^{-1} due to the C＝N stretching, C–N stretching of the second amine, the aromatic C＝C stretching vibration of the benzenoid and quinonoid rings, respectively (Cong et al., 2013). In the FT-IR spectra of the MoS$_2$/rGO binary composite, there is no obvious peak arisen from the vibration of oxygen containing functional groups on GO, which is attributed to the reduction of graphene oxide after hydrothermal treatment. The weak peak at about 500 cm^{-1} is assigned to MoS$_2$ vibration. Furthermore, the FT-IR spectra of MGP-50 show the obvious existence of all the PANI and MoS$_2$/rGO characteristic peaks. With the increasing weight percent of PANI, the intensities of the main characteristic PANI peaks in the MoS$_2$/rGO/PANI ternary composites all show an

increase. This indicated that the PANI was successfully coated on the surface of the MoS$_2$/rGO binary composite, which is helpful to improve the dispersibility of MoS$_2$/rGO/PANI ternary composites in the electrolyte.

The morphologies of the MoS$_2$/rGO binary composite and MoS$_2$/rGO/PANI ternary composites are shown in **Figure 3**. As
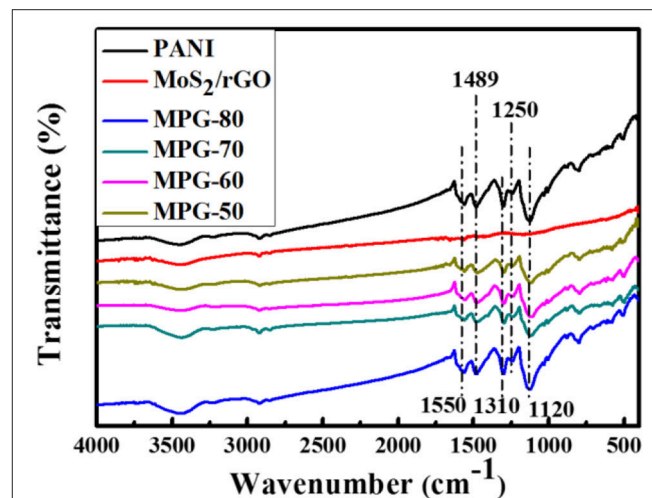

FIGURE 2 | FT-IR spectra of the PANI, MoS$_2$/rGO binary composite, and MoS$_2$/rGO/PANI ternary composites.
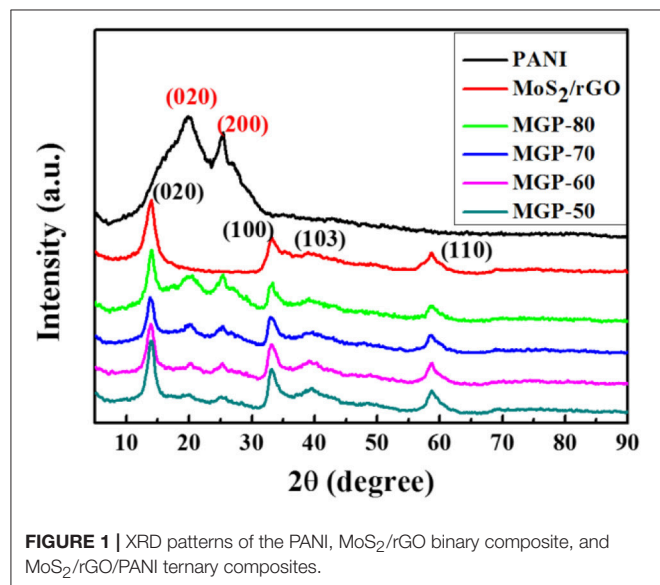

FIGURE 1 | XRD patterns of the PANI, MoS$_2$/rGO binary composite, and MoS$_2$/rGO/PANI ternary composites.
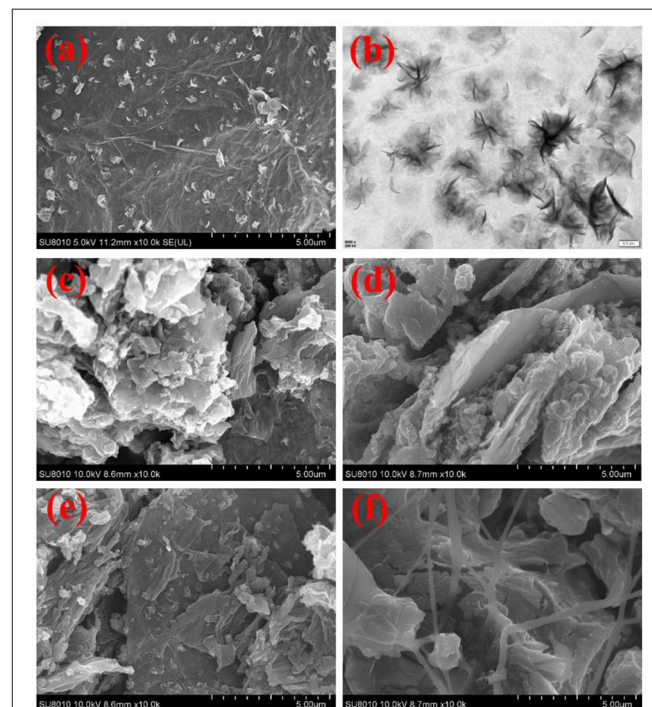

FIGURE 3 | SEM and TEM images of the MoS$_2$/rGO binary composite **(a,b)**, and SEM images of the MoS$_2$/rGO/PANI ternary composites [MRP-50 **(c)**, MRP-60 **(d)**, MRP-70 **(e)**, and MRP-80 **(f)**].

shown in **Figures 3a,b**, the MoS$_2$ nanosheets were well-scattered on the surface of rGO nanosheets to form hetero-layered architecture. The MoS$_2$/rGO binary composite as an attractive substrate can supply a large number of active sites for the growth of PANI. **Figures 3c–f** show the morphology of the MoS$_2$/rGO/PANI ternary composites with different weight percents of PANI. As shown in **Figure 3c**, the MGP-50 ternary composite shows that a well-defined and interconnected 3D network architecture. The PANI in a planar shape were

polymerized and attached onto the surface of the MoS$_2$/rGO binary composite due to the electrostatic interaction between negatively charged MoS$_2$/rGO and positively charged PANI (Luo et al., 2015). With the increased weight percent of PANI, PANI coated MoS$_2$/rGO assemble to generate a compact and laminated morphology so that the layer structure of MoS$_2$/rGO is not clearly seen due to the low content (**Figures 3d–f**). Such particular structure of the MoS$_2$/rGO/PANI ternary composites could increase the dispersion of PANI and improve
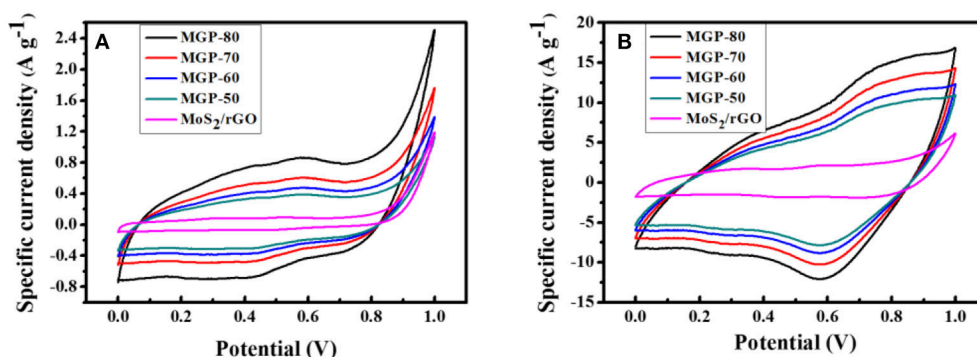
FIGURE 4 | CV curves for the MoS$_2$/rGO binary composite and MoS$_2$/rGO/PANI ternary composites at scan rates of **(A)** 2 and **(B)** 50 mV s^{-1}.
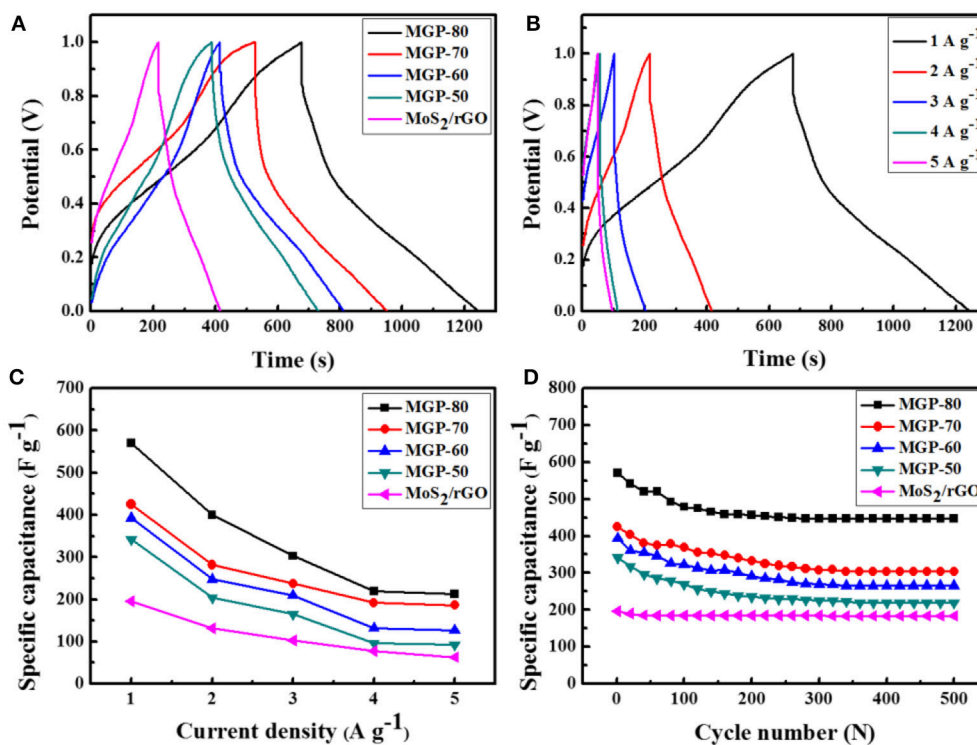
FIGURE 5 | (A) GCD curves of MoS$_2$/rGO binary composite and MoS$_2$/rGO/PANI ternary composites at a current density of 1 A g^{-1}, **(B)** GCD curves of the MGP-80 at different current densities, **(C)** the specific capacitance as a function of discharge current density; **(D)** cycle performance of the MoS$_2$ /rGO/PANI ternary composites at 1 A g^{-1}.

the interfaces of PANI with electrolyte, which might be beneficial for the improvement of electrochemical performance of the MoS$_2$/rGO/PANI ternary composite as electrode materials.

Electrochemical Performance of MoS$_2$/rGO/PANI Ternary Composites

Figure 4 shows the CV curves of the MoS$_2$/rGO binary composite and MoS$_2$/rGO/PANI ternary composites at scan rates of 2 and 5 mV s^{-1}. In the case of the MoS$_2$/rGO/PANI ternary composites, it can be found that CV loop exhibit larger areas under redox curve than the MoS$_2$/rGO binary composite, which indicates its higher specific capacitance. From the CV curves for the MoS$_2$/rGO/PANI ternary composites at different PANI content, it was noted that the MGP-80 electrode shows the largest rectangular curve corresponding to the highest capacitance among the four samples. The CV curves for the MGP80 at a low scan rate of 2 mV s^{-1} show severely distorted rectangular shapes as well as two conspicuous pairs of small, broad oxidation and reduction peaks, resulting from the co-contribution of electrical double-layer capacitance generated from MoS$_2$/rGO and pseudocapacitance arising from PANI (Wang et al., 2015). The redox peaks become less obvious, and the potential of the oxidation peak moves to higher potential while the potential of the reduction peak shifts to lower at a high scan rate of 50 mV s^{-1}. It should be noted that MoS$_2$/rGO/PANI ternary composites have fast ionic transport for charge-discharge operations, which results from synergetic effect of MoS$_2$/rGO and PANI.

The supercapacitance behavior of the MoS$_2$/rGO/PANI ternary composites was further investigated using GCD measurements, as shown in **Figure 5**. **Figure 5A** displays the GDC curves of the MoS$_2$/rGO,MoS$_2$/rGO/PANI with different amounts of PANI at a current density of 1 Ag^{-1}. It can be seen that the shapes of the GDC curves of ternary composites are similar to that of binary composite, which indicates that the ternary composite possesses the co-contribution of electrical double-layer capacitance and pseudo-capacitance. The ternary composites with different amounts of PANI exhibit a higher discharge time and lower IR drop than binary composite, which indicates that the introduction of PANI can enhance the capacitance and conductivity (Wang et al., 2013). The discharge time of the ternary composites increased with an increase amounts of PANI. The MGP-80 ternary composite exhibits the maximum discharge time. Furthermore, the GCD curves of the MRP-80 at different current densities from 1 to 5 A g^{-1} are shown in **Figure 5B**. It could be seen that with the increase of current density, the discharge time of the composite decreased due to partial accessibility for electrolyte ions within the active material at high currents. **Figure 5C** reveals the specific capacitances of the ternary composites at the current densities of 1, 2, 3, 4, and 5 Ag^{-1}. As can be observed, the capacitances of the MGP-80 were 570, 400, 303, 220, and 212 Fg^{-1}, respectively. **Figure 5D** shows the cycle stability of the ternary composite at a current density of 1 A g^{-1}. After 500 charging and discharging cycles, the specific capacitances of MPG-50, MPG-60, MPG-70
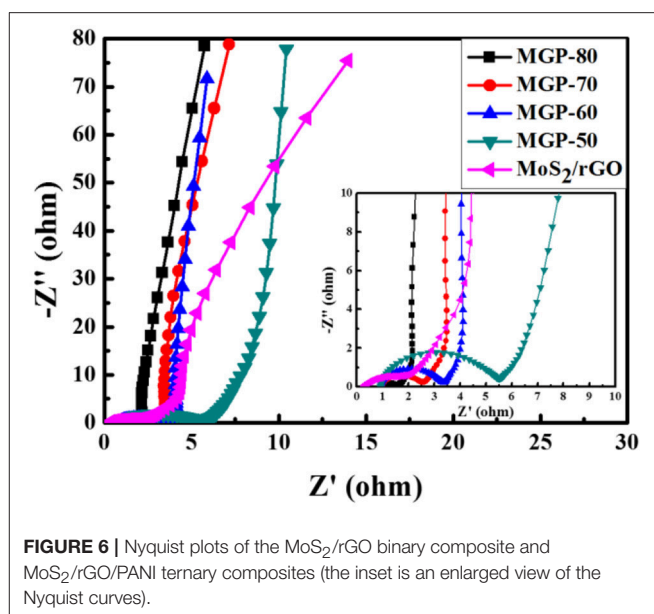

FIGURE 6 | Nyquist plots of the MoS$_2$/rGO binary composite and MoS$_2$/rGO/PANI ternary composites (the inset is an enlarged view of the Nyquist curves).

and MPG-80 retained 64.3, 67.7, 71.5, and 78.6% of the value of the first cycle, respectively. The good cycling stability of MPG-80 is ascribed to the fact that the synergistic effect between the MoS$_2$/rGO and PANI could relieve the volumetric shrinkage or swelling of PANI during the charge/discharge process (Dai et al., 2013).

EIS was carried out to describe the electrochemical process of the electrode/electrolyte interface. **Figure 6** shows the Nyquist plots of MoS$_2$/rGO binary composite and MoS$_2$/rGO/PANI ternary composites. In high-frequency regions, the intercept of the semicircle with the X-axis represents the equivalent series resistance (R$_s$) of the electrode materials, while the diameter of the semicircle corresponds to the charge transfer resistance (R$_{ct}$) (Sk et al., 2014). From the Nyquist plots, the R$_s$ of MoS$_2$/rGO binary composite and MoS$_2$/rGO/PANI ternary composites (MGP-50, MGP-60, MGP-70 and MGP-80) were 0.28, 0.90, 0.93, 0.97, and 1.03 Ω, respectively, indicating that the introduction of PANI could decrease the electrical conductivity of binary composite. However, R$_{ct}$ displays a opposite trend, probably because that the hierarchical structures of MoS$_2$/rGO/PANI ternary composites show the fast charge transfer rates and reflect a preferable electrochemical performance. In low frequency regions, the nearly parallel to imaginary axis of the lines show that MoS$_2$/rGO/PANI ternary composites have an ideal capacitive behavior. These results indicated that the ternary composite could improved charge storage and transportation within the electrode, which should be considered as a better electrode material (Liu et al., 2014).

CONCLUSIONS

MoS$_2$/rGO/PANI ternary composites with different amounts of PANI were successfully prepared by a two-stage

synthesis combing a hydrothermal method with *in situ* chemical oxidative polymerization, and their supercapacitor performance were further investigated using electrochemical measures. The introduction of PANI in the MoS$_2$/rGO binary composite not only hindered the agglomeration of MoS$_2$/rGO, but also resulted in a synergistic effect among these three components. MoS$_2$/rGO/PANI ternary composite with 80% PANI (MGP-80) showed the highest specific capacitance of 570 F g^{-1} at of 1 A g^{-1} which was comparatively larger than MoS$_2$/rGO binary composite (200 F g^{-1}). Furthermore, it was noticed that the specific capacitance of the MGP-80 composite retained more than 78.6% after 500 cycles at 1 A g^{-1}. All the evidences suggest that the MoS$_2$/rGO/PANI ternary composite is a high-performance electrode material for next-generation supercapacitors.

REFERENCES

Ataca, C., Sahin, H., and Ciraci, S. (2012). Stable, single-layer MX$_2$ transition-metal oxides and dichalcogenides in a honeycomb-like structure. *J. Phys. Chem. C* 116, 8983–8999. doi: 10.1021/jp212558p

Chen, W., Xia, C., and Alshareef, H. N. (2014). One-step electrodeposited nickel cobalt sulfide nanosheet arrays for high-performance asymmetric supercapacitors. *ACS Nano* 8, 9531–9541. doi: 10.1021/nn503814y

Cong, H. P., Ren, X. C., Wang, P., and Yu, S. H. (2013). Flexible graphene-polyaniline composite paper for high-performance supercapacitor. *Energ. Environ. Sci.* 6, 1185–1191. doi: 10.1039/c2ee24203f

Dai, C. S., Chien, P. Y., Lin, J. Y., Chou, S. W., Wu, W. K., Li, P. H., et al. (2013). Hierarchically structured Ni$_3$S$_2$/carbon nanotube composites as high performance cathode materials for asymmetric supercapacitors. *ACS Appl. Mater. Inter.* 5, 12168–12174. doi: 10.1021/am404196s

Dai, S., Zhao, B., Qu, C., Chen, D., Dang, D., Song, B., et al. (2017). Controlled synthesis of three-phase NixSy/rGO nanoflake electrodes for hybrid supercapacitors with high energy and power density. *Nano Energy* 33, 522–531. doi: 10.1016/j.nanoen.2017.01.056

da Silveira Firmiano, E. G., Rabelo, A. C., Dalmaschio, C. J., Pinheiro, A. N., Pereira, E. C., Schreiner, W. H., et al. (2014). Supercapacitor electrodes obtained by directly bonding 2D MoS$_2$ on reduced graphene oxide. *Adv. Energy Mater.* 4:1301380. doi: 10.1002/aenm.201301380

David, L., Bhandavat, R., and Singh, G. (2014). MoS$_2$/graphene composite paper for sodium-ion battery electrodes. *ACS Nano* 8, 1759–1770. doi: 10.1021/nn406156b

Dunn, B., Kamath, H., and Tarascon, J. M. (2011). Electrical energy storage for the grid: a battery of choices. *Science* 334, 928–935. doi: 10.1126/science.1212741

Huang, K. J., Wang, L., Liu, Y. J., Liu, Y. M., Wang, H. B., Gan, T., et al. (2013). Layered MoS$_2$-graphene composites for supercapacitor applications with enhanced capacitive performance. *Int. J. Hydrogen Energy* 38, 14027–14034. doi: 10.1016/j.ijhydene.2013.08.112

Khan, M., Yousaf, A. B., Chen, M. M., Wei, C. S., Wu, X. B., Huang, N. D., et al. (2016). Molybdenum sulfide/graphene-carbon nanotube nanocomposite material for electrocatalytic applications in hydrogen evolution reactions. *Nano Res.* 3, 837–848. doi: 10.1007/s12274-015-0963-z

Li, L., Wu, Z., Yuan, S., and Zhang, X. B. (2014). Advances and challenges for flexible energy storage and conversion devices and systems. *Energy Environ. Sci.* 7, 2101–2122. doi: 10.1039/c4ee00318g

Li, M., Cao, X. J., Zheng, S. R., and Qi, S. H. (2017). Ternary composites RGO/MoS$_2$@ Fe$_3$O$_4$: synthesis and enhanced electromagnetic wave absorbing performance. *J. Mater. Sci. Mater. Electron.* 22, 16802–16812. doi: 10.1007/s10854-017-7595-x

Liu, H., Qing, H. B., Li, Z. D., Han, Y. L., Lin, M., Yang, H., et al. (2017). A promising material for human-friendly functional wearable electronics. *Mat. Sci. Eng. R* 112, 1–22. doi: 10.1016/j.mser.2017.01.001

Liu, T., Finn, L., Yu, M., Wang, H., Zhai, T., Lu, X., et al. (2014). Polyaniline and polypyrrole pseudocapacitor electrodes with excellent cycling stability. *Nano Lett.* 14, 2522–2527. doi: 10.1021/nl500255v

Luo, J., Ma, Q., Gu, H. H., Zheng, Y., and Liu, X. Y. (2015). Three-dimensional graphene-polyaniline hybrid hollow spheres by layer-by-layer assembly for application in supercapacitor. *Electrochim. Acta* 173, 184–192. doi: 10.1016/j.electacta.2015.05.053

Qu, C., Zhang, L., Meng, W., Liang, Z., Zhu, B., Dang, D., et al. (2018). MOF-derived α-NiS nanorods on graphene as an electrode for high-energy-density supercapacitors. *J. Mater. Chem. A* 6, 4003–4012. doi: 10.1039/C7TA11100B

Sk, M. M., Yue, C. Y., and Jena, P. K. (2014). Facile growth of heparin-controlled porous polyaniline nanofiber networks and their application in supercapacitors. *RSC Adv.* 4, 5188–5197. doi: 10.1039/c3ra45774e

Thangappan, R., Kalaiselvam, S., Elayaperumal, A., Jayavel, R., Arivanandhan, M., Karthikeyan, R., et al. (2016). Graphene decorated with MoS$_2$ nanosheets: a synergetic energy storage composite electrode for supercapacitor applications. *Dalton Trans.* 45, 2637–2646. doi: 10.1039/C5DT04832J

Tong, Z. Q., Yang, Y. N., Wang, J. Y., Zhao, J. P., Su, B. L., and Li, Y. (2014). Layered polyaniline/graphene film from sandwich-structured polyaniline/graphene/polyaniline nanosheets for high-performance pseudosupercapacitors. *J. Mater. Chem. A* 2, 4642–4651. doi: 10.1039/C3TA14671E

Wang, G. X., Tang, Q. Q., Bao, H., Li, X. W., and Wang, G. C. (2013). Synthesis of hierarchical sulfonated graphene/MnO$_2$/polyaniline ternary composite and its improved electrochemical performance. *J. Power Sources* 241, 231–238. doi: 10.1016/j.jpowsour.2013.04.122

Wang, J., Wu, Z. C., Hu, K. H., Chen, X. Y., and Yin, H. B. (2015). High conductivity graphene-like MoS$_2$/polyaniline nanocomposites and its application in supercapacitor. *J. Alloy Compd.* 619, 38–43. doi: 10.1016/j.jallcom.2014.09.008

Wang, Y. X., Chou, S. L., Wexler, D., Liu, H. K., and Dou, S. X. (2014). High-performance sodium-ion batteries and sodium-ion pseudocapacitors based on MoS$_2$/graphene composites. *Chem. Eur. J.* 20, 9607–9612. doi: 10.1002/chem.201402563

Wu, Z., Li, L., Yan, J. M., and Zhang, X. B. (2017). Materials design and system construction for conventional and new-concept supercapacitors. *Adv. Sci.* 4:1600382. doi: 10.1002/advs.201600382

Xie, D., Wang, D. H., Tang, W. J., Xia, X. H., Zhang, Y. J., Wng, X. L., et al. (2016). Binder-free network-enabled MoS2-PPY-rGO ternary electrode for high capacity and excellent stability of lithium storage. *J. Power Sources* 307, 510–518. doi: 10.1016/j.jpowsour.2016.01.024

Yu, G. H., Xie, X., Pan, L. J., Bao, Z. N., and Cui, Y. (2013). Hybrid nanostructured materials for high-performance electrochemical capacitors. *Nano Energy* 2, 213–234. doi: 10.1016/j.nanoen.2012.10.006

Zhang, D. D., Zhao, D. L., Yao, R. R., and Xie, W. G. (2015). Enhanced mechanical properties of ammonia-modified graphene nanosheets/epoxy nanocomposites. *RSC Adv.* 5, 28098–28104. doi: 10.1039/C5RA0 0312A

Zhang, L. L., Zhao, X., Stoller, M. D., Zhu, Y., Ji, H., Murali, S., et al. (2012). Highly conductive and porous activated reduced graphene oxide films for high-power supercapacitors. *Nano Lett.* 12, 1806–1812. doi: 10.1021/nl20 3903z

Zhang, Q. B., Zhao, B. T., Wang, J. X., Qu, C., Sun, H. B., Zhang, K. L., et al. (2016). High-performance hybrid supercapacitors based on self-supported 3D ultrathin porous quaternary Zn-Ni-Al-Co oxide nanosheets. *Nano Energy* 28, 475–485. doi: 10.1016/j.nanoen.2016. 08.049

Zhao, B. T., Zhang, L., Zhang, Q. B., Chen, D. C., Cheng, Y., Deng, X., et al. (2018). Rational design of nickel hydroxide-based nanocrystals on graphene for ultrafast energy storage. *Adv. Energy Mater.* 8:1702247. doi: 10.1002/aenm.201702247